Depth sectioning combined with atom-counting in HAADF STEM to retrieve the 3D atomic structure

Depth sectioning combined with atom-counting in HAADF STEM to retrieve the 3D atomic structure

M. Alania[a], T. Altantzis[a], A. De Backer[a], I. Lobato[a], S. Bals[a], S. Van Aert[a,*]

[a]*Electron Microscopy for Materials Science (EMAT), University of Antwerp, Groenenborgerlaan 171, 2020 Antwerp, Belgium*

Abstract

Aberration correction in scanning transmission electron microscopy (STEM) has greatly improved the lateral and depth resolution. When using depth sectioning, a technique during which a series of images is recorded at different defocus values, single impurity atoms can be visualised in three dimensions. In this paper, we investigate new possibilities emerging when combining depth sectioning and precise atom-counting in order to reconstruct nanosized particles in three dimensions. Although the depth resolution does not allow one to precisely locate each atom within an atomic column, it will be shown that the depth location of an atomic column as a whole can be measured precisely. In this manner, the morphology of a nanoparticle can be reconstructed in three dimensions. This will be demonstrated using simulations and experimental data of a gold nanorod.

Keywords: STEM, three-dimensional imaging, depth sectioning, quantitative electron microscopy, atom-counting

1. Introduction

In scanning transmission electron microscopy (STEM), an electron beam is focused to a fine probe that is scanned across the sample in a two-dimensional (2D) raster [1]. For each probe position, the electrons scattered towards the detector are integrated and displayed as a function of probe position. A key

---

*Corresponding author
Email address:* `sandra.vanaert@uantwerpen.be` (S. Van Aert)

imaging mode is high angle annular dark field (HAADF) STEM, in which an annular detector is used with a collection range outside the illumination cone. The high-angle scattering thus detected is dominated by Rutherford and thermal diffuse scattering. Therefore, the HAADF signal emitted by each atom contributes incoherently [2, 3] and scales approximately proportional with the square of the atomic number Z [3, 4].

Thanks to recent progress in aberration correction, atomic resolution can nowadays be achieved on a routine basis in 2D in HAADF STEM [5, 6] enabling structure characterisation and chemical mapping at the atomic scale [7, 8]. However, one should never forget that these results are only 2D projections of a three-dimensional (3D) object. Therefore, electron tomography has evolved into a standard technique to investigate the morphology of nanomaterials. Recently, the resolution was pushed to the atomic level using different techniques. Most of the results were obtained by combining a limited number or a more elaborate tilt series with advanced reconstruction algorithms [9, 10, 11]. Although these approaches enable one to measure atom positions and the chemical nature in nanoparticles atom-by-atom, it is far from straightforward to obtain similar results for samples with a slab-like geometry such as thin films or 2D self-assembled structures. This is related to the increasing projected thickness of the sample when reaching tilt angles higher than e.g. 40°. An alternative technique to visualise the 3D atomic structure is the use of so-called depth sectioning or optical sectioning [12, 13]. The development of aberration correctors in STEM has indeed led to a considerable reduction in the microscope depth of field, which may be just a few nanometres. This benefit is explored in depth sectioning where a so-called through-focal series of images of the sample is acquired. Similar as in light microscopy [14], 3D structural information can then directly be extracted from images recorded at different defocus values or use can be made of more advanced reconstruction algorithms [15].

Depth sectioning has successfully been applied to detect individual dopant atoms [12, 13] or to identify complex dislocations [16, 17]. Unfortunately, the vertical probe size is of the order of several nm, thus far too large to visualise all individual atoms in a nanostructure when using this technique [13, 18, 19]. Moreover, non-linear interactions complicate the interpretation [20]. However, we show in this paper that the combination of depth sectioning in HAADF STEM and precise atom-counting [9, 21, 22, 23] can be used to reconstruct nanosized particles in 3D. Indeed, when the number of atoms is measured in each atomic column, the problem of reconstructing the 3D

2

atomic structure can be reduced to determine the depth location of all atomic columns from a through-focal series. The depth locations are then considered as unknown structure parameters which can be determined from a focal series using model fitting. For experimentally acquired images, model fitting never results in a perfect match in the presence of noise and therefore puts a limit to the statistical precision with which the depth location can be estimated. Using the principles of statistical parameter estimation theory, we will investigate in section 2 how precise one could locate the individual atoms in 3D when using depth sectioning and what precision can be attained when measuring the depth location of an atomic column with known number of atoms. Next, in section 3, a reconstruction algorithm is proposed that can be used to determine the 3D morphology from a focal series of HAADF STEM images. Moreover, a proof of concept is presented where we determine the morphology of a gold nanorod. These results are compared with 3D reconstructions based on projection images acquired along different tilt angles. In section 4, conclusions are drawn.

2. Statistical measurement precision

2.1. The Cramér-Rao lower bound CRLB

Ultimately, the precision with which unknown structure parameters can be estimated, such as the 3D locations of atoms or the depth location of an atomic column, is limited by noise. Indeed, due to noise, the pixel values that constitute the experimental images will fluctuate randomly from experiment to experiment. These pixel values, which we will from now on refer to as observations, can be modelled as random variables, characterized by a joint probability function (PF). In a STEM experiment the observations are counting results, for which the PF can be modelled as a Poisson distribution. Based on the PF, an expression for the highest attainable precision with which structure parameters of the sample under study can be estimated in an unbiased way can be derived using the concept of Fisher information [24, 25]. This expression defines a lower bound on the parameter variance and is known as the Cramér-Rao lower bound (CRLB).

Consider a set of stochastic observations w_{kl}^j, $k = 1, ..., K$, $l = 1, ..., L$, and $j = 1, ..., J$. Then the vector w defined as

$$w = (w_{11}^1, ... w_{KL}^J)^T \tag{1}$$

3

represents the column vector of these observations of dimension $K \times L \times J$, where $K \times L$ corresponds to the dimensions of each image in a focal series containing J images. If the observations are assumed to be statistically independent, Poisson distributed variables, the probability that the observation w_{kl}^j is equal to ω_{kl}^j is given by [26]

$$\frac{\left(\lambda_{kl}^j\right)^{\omega_{kl}^j}}{\omega_{kl}^j!} \exp\left(-\lambda_{kl}^j\right) \tag{2}$$

with λ_{kl}^j the expected number of detected electrons at pixel (k, l) at the jth defocus value. The expected number of detected electrons per pixel position (k, l) at the jth defocus value equals

$$\lambda_{kl}^j = f_{kl}^j \frac{I\tau}{e} \tag{3}$$

with f_{kl}^j the fraction of electrons expected to be recorded by the detector, I the probe current in ampere, τ the recording dwell time for one pixel, and $e = 1.6 \times 10^{-19}$ C the electron charge. These expectation values can be accurately simulated using the multislice method. When assuming statistically independent observations, the probability $P(\omega; \beta)$ that a set of observations is equal to $\omega = (\omega_{11}^1, ...\omega_{KL}^J)^T$ is the product of all the probabilities described by Eq. (2):

$$P(\omega; \beta) = \prod_{j=1}^{J} \prod_{k=1}^{K} \prod_{l=1}^{L} \frac{\left(\lambda_{kl}^j\right)^{\omega_{kl}^j}}{\omega_{kl}^j!} \exp\left(-\lambda_{kl}^j\right). \tag{4}$$

This function is the joint PF of the observations. Since the expectation values depend on the choice of the structure of the object under study, the unknown structure parameters β enter $P(\omega; \beta)$ via λ_{kl}^j.

The expression for the joint PF enables one to compute the CRLB. The CRLB follows from the concept of the Fisher information. The Fisher information matrix F for estimation of a set of unknown structure parameters β is defined as

$$F = -E\left[\frac{\partial^2 \ln P(\omega; \beta)}{\partial \beta \partial \beta^T}\right] \tag{5}$$

where $P(\omega; \beta)$ is the joint PF of the observations given by Eq.(4) and

$$\frac{\partial^2 \ln P(\omega; \beta)}{\partial \beta \partial \beta^T} \tag{6}$$

4

is the Hessian matrix of $\ln P(\omega; \beta)$ of which the $(p, q)th$ element is defined as:

$$\frac{\partial^2 lnP(\omega; \beta)}{\partial \beta_p \partial \beta_q} \tag{7}$$

where β_p and β_q correspond to the p and qth element of the vector β, respectively. The elements $F(p, q)$ may be calculated explicitly using Eqs.(3)-(7) [27]:

$$F(p, q) = \sum_{j=1}^{J} \sum_{k=1}^{K} \sum_{l=1}^{L} \frac{1}{\lambda_{kl}^j} \frac{\partial \lambda_{kl}^j}{\partial \beta_p} \frac{\partial \lambda_{kl}^j}{\partial \beta_q}. \tag{8}$$

It is important to note that the dimension of the Fisher information matrix depends on the number of parameters to be estimated. When considering the problem of estimating all position coordinates along the depth direction of a set of N atoms in an isolated column, $\beta = (\beta_{z1}, \beta_{z2}, ..., \beta_{zN})$, F is a $N \times N$ matrix. When considering the problem of only estimating the depth location β_d of an isolated column with known number of atoms and known distance between the atoms, F is a scalar.

Suppose that $\hat{\beta}$ is an unbiased estimator of β. The Cramér-Rao inequality then states that [28]

$$\text{cov}(\hat{\beta}, \hat{\beta}) \geq F^{-1} \tag{9}$$

where $\text{cov}(\hat{\beta}, \hat{\beta})$ is the variance-covariance matrix of the estimator $\hat{\beta}$, defined by its $(p, q)th$ element $\text{cov}(\hat{\beta}_p, \hat{\beta}_q)$. Its diagonal elements are thus the variances of the elements of $\hat{\beta}$. The matrix F^{-1} is called the Cramér-Rao lower bound on the variance of $\hat{\beta}$. The Cramér-Rao inequality (9) expresses that the difference between the left-hand and right-hand member is positive semi-definite. A property of a positive semi-definite matrix is that its diagonal elements cannot be negative. This means that the diagonal elements of $\text{cov}(\hat{\beta}, \hat{\beta})$ will always be larger than or equal to the corresponding diagonal elements of the inverse of the Fisher information matrix. Therefore, the diagonal elements of F^{-1} define lower bounds on the variances of the elements of $\hat{\beta}$

$$\text{var}(\hat{\beta}_p) \geq \sigma^2_{\beta_{zp}} = F^{-1}(p, p) \tag{10}$$

where $F^{-1}(p, p)$ is the (p, p)th element of the inverse of the Fisher information matrix.

2.2. Numerical results

The expression for the CRLB given in section 2.1 enables one to predict the highest attainable precision with which the individual atoms within an atomic column or the depth location of an atomic column can be estimated. Based on realistic image simulations, one can compute the expectation values λ_{kl}^{j} and the derivatives with respect to the unknown structure parameters. In this manner, the elements of the Fisher information matrix can be computed using Eq.(8). Next, the right-hand side of expression (10) defines the attainable precision with which the unknown parameters can be estimated.

In this study, the multislice algorithm [29] has been used to compute the expectation values λ_{kl}^{j} using the MULTEM software [30, 31]. An isolated column of 10 gold atoms has been assumed, which is aligned along the optical axis and where the distance between the atoms equals 4.08 Å. The settings used for the multislice simulations are summarised in Table 1. Furthermore, the finite source size has been modelled by convolving the resulting image with a Gaussian distribution. Derivatives of λ_{kl}^{j} with respect to the position coordinates $\beta_{z1},...,\beta_{zN}$ have been computed using the finite difference quotient by simulating images with the p-th atom shifted 10 pm over and under the nominal position. Figure 1 shows (x, z) slices of these derivatives. The attainable precision can now be expressed in terms of the lower bound on the standard deviation $\sigma_{\beta_{zp}}$, which is defined by the square root of the right-hand side of expression (10). Table 2 summarises the results for each atom in the column. From these numbers, it follows that the standard deviation is only in the nanometer range and consequently the attainable precision is very low. In practice, this means that even under ideal conditions, precise estimates of the positions of individual atoms along the depth direction cannot be expected.

Although the results of Table 2 show that precise atomic scale measurements of the displacements of atoms in a nanoparticle in 3D (e.g. due to strain) are not within reach when using depth sectioning, *a priori* information can be introduced in the estimation problem. When the number of atoms in each atomic column is estimated and if the distance between the atoms is known, the number of unknown parameters is significantly reduced. In this manner, the unknown parameters to be estimated are the depth locations of all atomic columns. For an isolated column, the Fisher information matrix then reduces to a scalar. In a similar manner as before, the lower bound on the standard deviation $\sigma_{\beta_{d}}$ with which the depth location can be estimated has been computed, which is defined by the square root of the right-hand

6

Table 1: Overview of simulation settings.

|	
Slice thickness	4.08 Å
Debye-Waller factor	0.63 Å^2
Acceleration voltage	300 kV
Defocus range	[-200,200] Å
Defocus step	10 Å
Number of focal images	41
Spherical aberration C_3	0 mm
Convergence angle	21 mrad
Detector collection range	[48-180] mrad
FWHM of the source image	0.7 Å
Pixel size of simulated image	0.1 Å
Pixel size to sample atomic potential	0.0342 Å
Incident electron dose per image	9612 e$^-$/Å^2
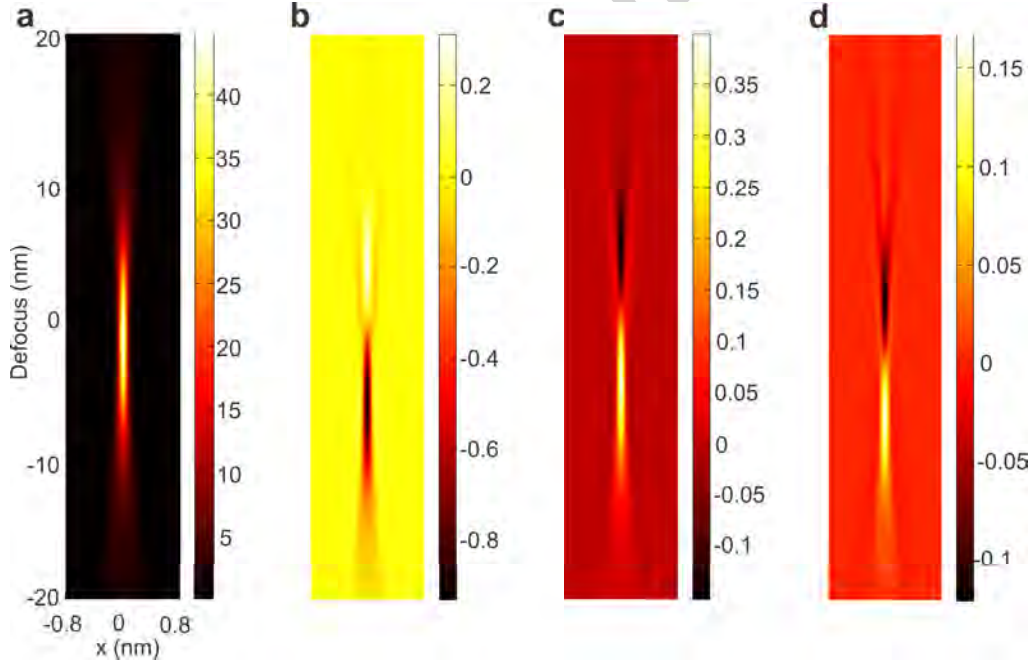
Figure 1: Two-dimensional (x, z) depth profile of a simulated focal series of a 10 atoms thick gold column and its derivatives. (a) Simulated focal series λ_{kl}^j. (b) Derivative $\partial \lambda_{kl}^j / \partial \beta_{z1}$ with respect to the first atom. (c) Derivative $\partial \lambda_{kl}^j / \partial \beta_{z2}$ with respect to the second atom. (d) Derivative $\partial \lambda_{kl}^j / \partial \beta_{z7}$ with respect to the seventh atom.

7

atom number p	1	2	3	4	5	6	7	8	9	10
$\sigma_{\beta_{zp}}$ (nm)	4.10	4.42	4.48	3.70	4.46	4.25	5.81	3.42	5.48	3.06

Table 2: Lower bound on the standard deviation $\sigma_{\beta_{zp}}$ of the position coordinate β_{zp} along the depth direction of a 10 atoms thick gold column, where $p = 1$ and $p = 10$ correspond to the atom at the top and at the bottom of the column, respectively.
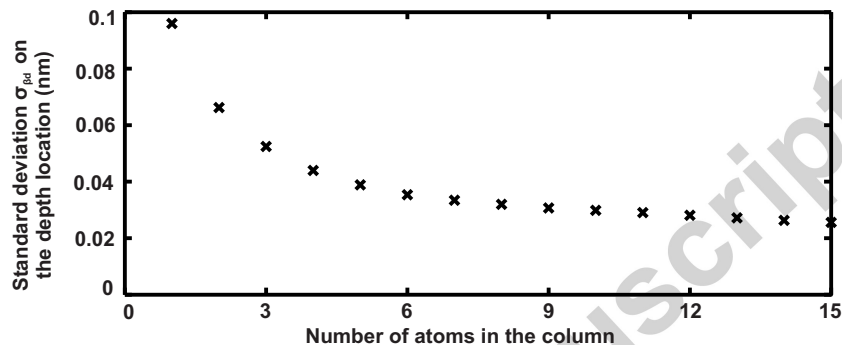

Figure 2: Lower bound on the standard deviation σ_{β_d} with which the depth location of an atomic column can be estimated for increasing number of gold atoms in an isolated column.

side of expression (10). This has been done for an increasing number of gold atoms in a column. The results are shown in figure 2 demonstrating that the attainable precision with which the depth location of an atomic column can be estimated is in the sub-Å scale and improves with increasing number of atoms in the column.

3. 3D atomic scale reconstruction of nanosized structures

The results shown in section 2 theoretically demonstrate that under realistic experimental conditions, the attainable precision with which individual atoms can be located using depth sectioning is very low. However, when incorporating *a priori* knowledge concerning the number of atoms and the inter-atomic distance, only the depth location needs to be estimated for which a precision in the sub-Å scale is predicted. In this section, an algorithm is presented to actually estimate the depth location of atomic columns for crystals consisting of a single type of element. In this manner, we will reconstruct the 3D morphology of a gold nanorod based on an experimental through-focal series of HAADF STEM images.

8

3.1. Reconstruction algorithm

The reconstruction algorithm can be divided into five steps:

1. A through-focal series of HAADF STEM images is acquired.
2. The images are corrected for drift using an iterative phase-correlation method [32]. This results in a corrected 3D stack of images as shown in figure 3a, where the z-axis corresponds to the depth direction. Note that the atomic columns are not resolved in the top image, since this is an out-of-focus image.
3. The 2D x, y-position coordinates and the number of atoms are estimated for each atomic column using StatSTEM [9, 21, 22, 23, 33].
4. For each atomic column, the depth location is determined. Therefore, average intensities are first determined for each column as a function of defocus. This is demonstrated in figure 3b. Figure 3b shows the experimental intensities as a function of defocus averaged around a column position indicated by the red dot in figure 3a. This results in the blue crosses shown in figure 3b. Next, the peak location is determined by fitting the parameters of a 1-dimensional Gaussian function to these experimental values using the Gaus-Newton method for non-linear least-squares estimation. The estimated Gaussian function is shown in black in figure 3b. However, since the peak location does not correspond to the center of mass of the column, a correction is applied in order to determine the depth location based on a simulated through-focal series using the MULTEM software [30, 31].
5. Finally, a 3D atomic reconstruction is obtained where the x, y, z-position coordinates of all atoms are relaxed to positions of a known crystallographic structure.

From the description of the reconstruction algorithm, it is clear that the experimental intensities are analysed on an atomic column-by-atomic column basis. It is therefore assumed that the focal series images can be described as a linear superposition of the images of the individual atomic columns. Although cross-talk is not taken into account in this manner, this approximation works well for thin enough samples [34].

3.2. Experimental 3D reconstruction of a Au nanorod

Using depth sectioning, the edge of a Au nanorod has been reconstructed in 3D. The shape of the rod is expected to be close to cylindrical with a width of 17.5 nm and a length of 62.2 nm.
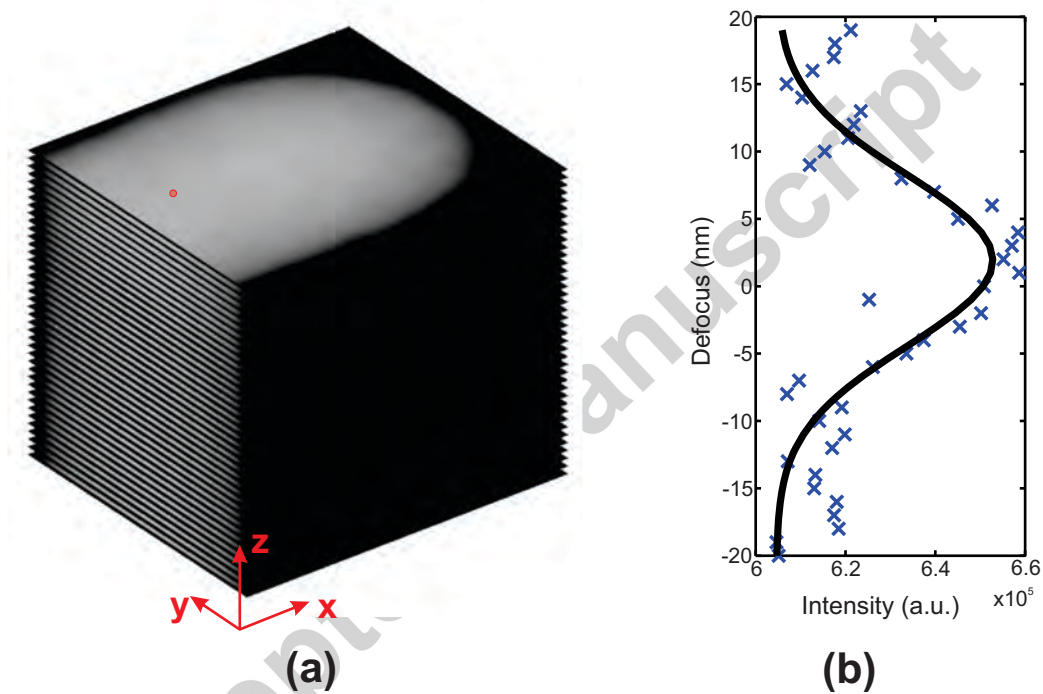
9

Figure 3: Illustration of the different steps used in the reconstruction algorithm. (a) 2D focal series of STEM images of a Au nanorod taken along the [100] zone-axis, where the z-axis corresponds to the depth direction. (b) Experimental intensities averaged around a column position, indicated by the red dot in figure 3a, as a function of defocus are shown by means of blue crosses together with a fitted Gaussian function in black to determine the peak location.

10

Figure 3a shows a through-focal series of HAADF STEM images of the tip of the Au nanorod along the [100] zone-axis, which has been acquired using a double aberration corrected cubed FEI Titan 50-80 electron microscope operated at 300 kV. The experimental settings are as follows: dwell time 10 μs, pixel size 51 pm, defocus step 1 nm, probe semi-convergence angle 21 mrad, 48-180 mrad detector collection range, and aberrations corrected up to 5th order. It is important to note that the incident electron dose per image is in good agreement with the dose used for the simulations. In addition to the focal series, a single atomic resolution HAADF STEM image has been acquired along the [110] zone-axis and a low magnification HAADF STEM tomography series have been taken in order to validate the 3D atomic reconstruction. The tomography series has been acquired with a tilt range from -74° to +74° and a tilt increment of 2° using a Fischione 2020 single tilt tomography holder. A 3D reconstruction with a resolution in the nanometer range has been obtained using the Simultaneous Iterative Reconstruction Technique (SIRT) implemented in the ASTRA toolbox [35].

The 3D reconstruction algorithm outlined in section 3.1 has been used in order to reconstruct the 3D atomic structure from the experimental focal series. The number of atoms in each atomic column (step 3) has been determined based on so-called scattering cross-sections resulting from the average of 8 central images of the focal series [9, 21, 22, 23]. This averaged projection image is shown in figure 4(a). The scattering cross-sections, corresponding to the total intensity of electrons scattered by the atomic columns, can indeed be shown to be robust for imaging parameters including defocus [36] validating this approach. The atom-counting results are shown in figure 4(b). Based on these counts and assuming that the atoms are located at positions of an FCC structure, the depth location of each atomic column has been determined. The results are summarised in figure 5. Figures 5a-c show a projection of the 3D low-resolution tomography reconstruction, a 2D STEM image, and a projection of the 3D depth sectioning reconstruction, respectively, along the [100] zone-axis. In figures 5d-f, these are shown along the [110] zone-axis. The accuracy of the depth sectioning reconstruction is demonstrated by comparing figure 5f with figures 5d and e showing that the overall shape of the particle can be reconstructed. However, local differences as well as non-physical fluctuations at the surface can not be avoided and reflect the limited precision with which the depth location can be determined.
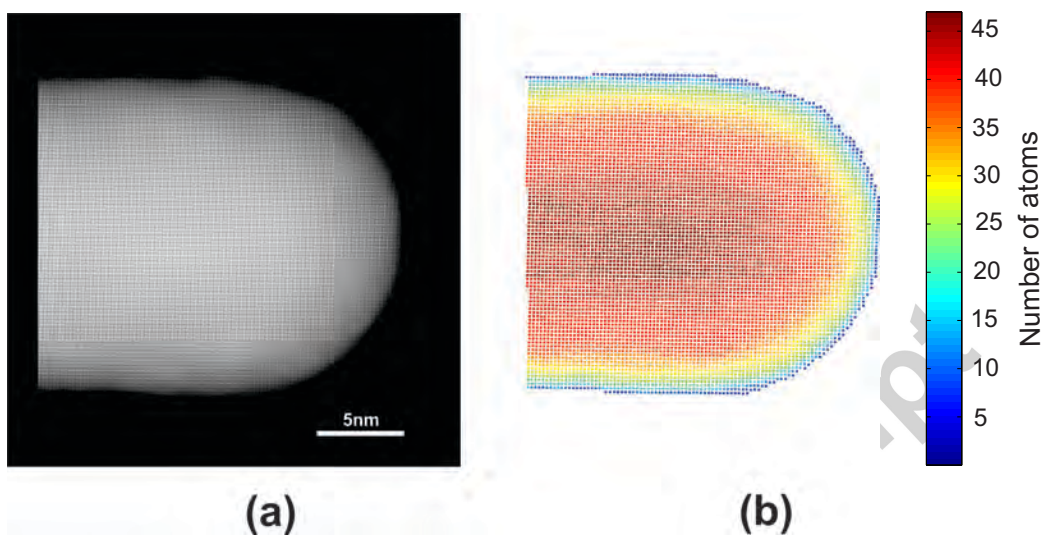
11

Figure 4: (a) Averaged projection image of the Au nanorod determined from the average of the 8 central images of the focal series acquired along the [100] zone axis. (b) Atom-counting results.
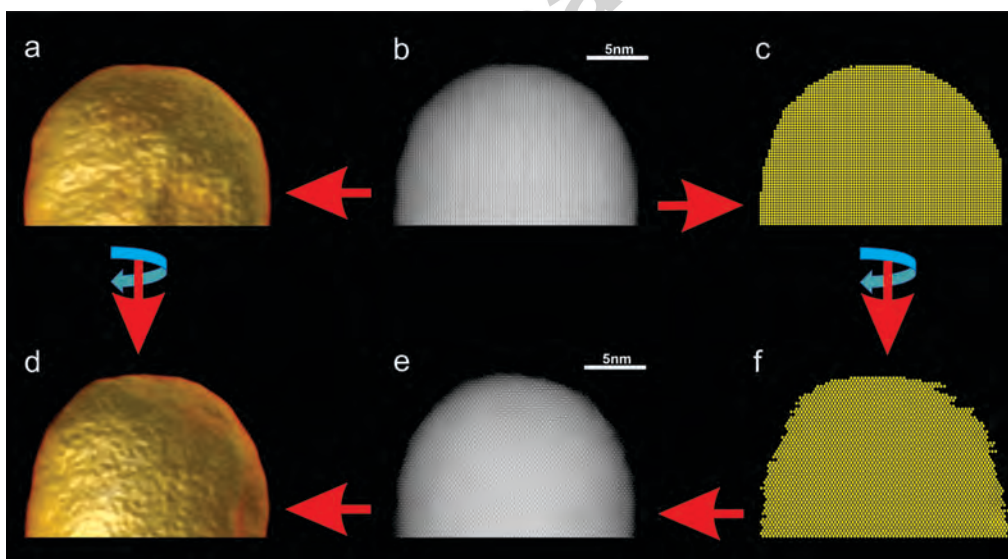

Figure 5: (a) 3D low-resolution tomography reconstruction along [100]. (b) 2D STEM projection image acquired along a [100] zone-axis. (c) 3D depth sectioning reconstruction viewed along [100], based on a focal series acquired along [100]. (d) 3D low-resolution tomography reconstruction along [110]. (e) 2D STEM projection image acquired along a [110] zone-axis. (f) 3D depth sectioning reconstruction viewed along [110], based on a focal-series acquired along [100].

12

4. Conclusion

In this paper, the use of depth sectioning in aberration corrected HAADF STEM for 3D atomic reconstruction has been investigated. Using the concept of the Cramér-Rao lower bound, the attainable precision with which individual atoms can be located along the depth direction has been predicted. It is shown that under realistic conditions, the standard deviation is large as compared to the interatomic distance thus demonstrating that the attainable precision is low. It is expected that this precision improves when using a larger illumination angle on condition that aberration correctors exist that provide a flat phase area of the Ronchigram for this larger convergence angle [37]. However, when incorporating knowledge concerning the crystal structure and using quantitative methods enabling one to precisely determine the number of atoms in each atomic column, the problem reduces to locating the depth location of each atomic column. Under realistic experimental settings, the precision with which the depth location can be determined is in the sub-Å range. Based on this observation, a simple but efficient reconstruction algorithm has been proposed and used to experimentally reconstruct the tip of a gold nanorod. In this manner, the 3D shape of the rod could be reconstructed. This work can be considered as a first proof of principle, but we expect that our methodology will be of great value for a broad range of nanosystems including thin films and 2D self-assembled nanomaterials. Recent advances in atom-counting for heterogeneous nanostructures [38] in combination with the design of new aberration correctors that will allow the use of a larger illumination angle [37], will open up new possibilities for measuring 3D surface morphology, thickness, top/surface atomic structures, point defects in bulk materials, and even depth-sensitive spectroscopy for hetero-nanostructures.

5. Acknowledgement

[1] A. V. Crew, J. Wall, L. M. Welter, A high-resolution scanning transmission electron microscope, J. Appl. Phys. 39 (1968) 5861 – 5868.

[2] R. F. Loane, P. Xu, J. Silcox, Incoherent imaging of zone-axis crystals with ADF STEM, Ultramicroscopy 40 (1992) 121.

[3] P. Hartel, H. Rose, C. Dinges, Conditions and reasons for incoherent imaging in STEM, Ultramicroscopy 63 (1996) 93 – 114.

[4] P. D. Nellist, S. J. Pennycook, The principles and interpretation of annular dark-field Z-contrast imaging, Vol. 113 of Advances in Imaging and Electron Physics, 2000, pp. 147–203.

[5] P. E. Batson, N. Dellby, O. L. Krivanek, Sub-angstrom resolution using aberration corrected electron optics, Nature 418 (2002) 617 – 620.

[6] P. D. Nellist, M. F. Chisholm, N. Dellby, O. L. Krivanek, M. F. Murfitt, Z. S. Szilagyi, A. R. Lupini, A. Y. Borisevich, W. H. Sides Jr., S. J. Pennycook, Direct sub-angstrom imaging of a crystal lattice, Science 305 (2004) 1741. doi:10.1126/science.1100965.

[7] S. Van Aert, J. Verbeeck, R. Erni, S. Bals, M. Luysberg, D. Van Dyck, G. Van Tendeloo, Quantitative atomic resolution mapping using high-angle annular dark field scanning transmission electron microscopy, Ultramicroscopy 109 (2009) 1236 – 1244.

[8] T. Grieb, K. Mueller, R. Fritz, V. Grillo, M. Schowalter, K. Volz, A. Rosenauer, Quantitative chemical evaluation of dilute GaNAs using ADF STEM: Avoiding surface strain induced artifacts, Ultramicroscopy 129 (2013) 1–9.

[9] S. Van Aert, K. J. Batenburg, M. D. Rossell, R. Erni, G. Van Tendeloo, Three-dimensional atomic imaging of crystalline nanoparticles, Nature 470 (7334) (2011) 374–377.

[10] B. Goris, S. Bals, W. Van den Broek, E. Carbo-Argibay, S. Gomez-Grana, L. M. Liz-Marzàn, G. Van Tendeloo, Atomic-scale determination of surface facets in gold nanorods, Nature Materials 11 (11) (2012) 930–935.

[11] M. Scott, C.-C. Chen, M. Mecklenburg, C. Zhu, R. Xu, P. Ercius, U. Dahmen, B. Regan, J. Miao, Electron tomography at 2.4-angstrom resolution, Nature 483 (7390) (2012) 444–447.

[12] K. van Benthem, A. R. Lupini, M. Kim, H. S. Baik, S. Doh, J.-H. Lee, M. P. Oxley, S. D. Findlay, L. J. Allen, J. T. Luck, S. J. Pennycook, Three-dimensional imaging of individual hafnium atoms inside a semiconductor device, Applied Physics Letters 87 (2005) 034104.

[13] K. van Benthem, A. R. Lupini, M. P. Oxley, S. D. Findlay, L. J. Allen, S. J. Pennycook, Three-dimensional ADF imaging of individual atoms by through-focal series scanning transmission electron microscopy, Ultramicroscopy 106 (11-12) (2006) 1062 – 1068.

[14] T. Wilson, Confocal microscopy, Academic Press, London, 1990.

[15] W. Van den Broek, S. Van Aert, D. Van Dyck, A model based reconstruction technique for depth sectioning with scanning transmission electron microscopy, Ultramicroscopy 110 (5) (2010) 548 – 554.

[16] P. B. Hirsch, J. G. Lozano, S. Rhode, M. K. Horton, M. A. Moram, S. Zhang, M. J. Kappers, C. J. Humphreys, A. Yasuhara, E. Okunishi, P. D. Nellist, The dissociation of the [a + c] dislocation in GaN, Philosophical Magazine 93 (2013) 3925 – 3938.

[17] H. Yang, J. G. Lozano, T. J. Pennycook, L. Jones, P. B. Hirsch, P. D. Nellist, Imaging screw dislocations at atomic resolution by aberration-corrected electron optical sectioning, Nature Communications 6 (2015) 7266.

[18] H. L. Xin, D. A. Muller, Aberration-corrected ADF-STEM depth sectioning and prospects for reliable 3D imaging in S/TEM, J. Electron Microsc. 58 (3) (2009) 157–165.

[19] E. C. Cosgriff, A. J. D'Alfonso, L. J. Allen, S. D. Findlay, A. I. Kirkland, P. D. Nellist, Three-dimensional imaging in double aberration-corrected

15

scanning confocal electron microscopy, part I: Elastic scattering, Ultramicroscopy 108 (12) (2008) 1558–1566.

[20] E. C. Cosgriff, P. D. Nellist, A Bloch wave analysis of optical sectioning in aberration-corrected STEM, Ultramicroscopy 107 (8) (2007) 626 – 634.

[21] S. Van Aert, A. De Backer, G. T. Martinez, B. Goris, S. Bals, G. Van Tendeloo, A. Rosenauer, Procedure to count atoms with trustworthy single-atom sensitivity, Phys. Rev. B 87 (2013) 064107.

[22] A. De Backer, G. T. Martinez, A. Rosenauer, S. Van Aert, Atom counting in HAADF STEM using a statistical model-based approach: Methodology, possibilities, and inherent limitations, Ultramicroscopy 134 (2013) 23 – 33.

[23] A. De Backer, G. T. Martinez, K. E. MacArthur, L. Jones, A. Bch, P. D. Nellist, S. Van Aert, Dose limited reliability of quantitative annular dark field scanning transmission electron microscopy for nano-particle atom-counting, Ultramicroscopy 151 (2015) 56–61. doi:10.1016/j.ultramic.2014.11.028.

[24] A. van den Bos, A. J. den Dekker, Resolution reconsidered - conventional approaches and an alternative, Advances in Imaging and Electron Physics 117 (2001) 241–360, San Diego: Academic Press. doi:10.1016/S1076-5670(01)80114-2.

[25] A. J. den Dekker, S. Van Aert, A. van den Bos, D. Van Dyck, Maximum likelihood estimation of structure parameters from high resolution electron microscopy images. Part I: A theoretical framework, Ultramicroscopy 104 (2) (2005) 83 – 106.

[26] A. M. Mood, F. A. Graybill, D. C. Boes, Introduction to the Theory of Statistics, 3rd Edition, McGraw-Hill Book Company, 1974.

[27] S. Van Aert, A. J. den Dekker, D. Van Dyck, A. van den Bos, Optimal experimental design of STEM measurement of atom column positions, Ultramicroscopy 90 (4) (2002) 273 – 289.

[28] M. G. Kendall, A. Stuart, The Advanced Theory of Statistics: In three volumes. Volume 2. Inference and Relationship (1967).

[29] E. J. Kirkland, Advanced Computing in Electron Microscopy, Plenum Press, New York, 1998.

[30] I. Lobato, D. Van Dyck, Improved multislice calculations for including higher-order Laue zones effects, Ultramicroscopy 119 (2012) 63 – 71.

[31] I. Lobato, S. Van Aert, J. Verbeeck, Progress and new advances in simulating electron microscopy datasets using MULTEM, Ultramicroscopy 168 (2016) 17–27.

[32] A. Alba, R. M. Aguilar-Ponce, J. F. Vigueras-Gómez, E. Arce-Santana, Phase correlation based image alignment with subpixel accuracy, in: Advances in Artificial Intelligence, Springer, 2012, pp. 171–182.

[33] A. De Backer, K. H. W. van den Bos, W. Van den Broek, J. Sijbers, S. Van Aert, StatSTEM: An efficient approach for accurate and precise model-based quantification of atomic resolution electron microscopy images, Ultramicroscopy 171 (2016) 104–116.

[34] G. T. Martinez, A. Rosenauer, A. De Backer, J. Verbeeck, S. Van Aert, Quantitative composition determination at the atomic level using model-based high-angle annular dark field scanning transmission electron microscopy, Ultramicroscopy 137 (2014) 12 – 19.

[35] W. Van Aarle, W. J. Palenstijn, J. De Beenhouwer, T. Altantzis, S. Bals, K. J. Batenburg, J. Sijbers, The ASTRA toolbox: a platform for advanced algorithm development in electron tomography, Ultramicroscopy 157 (2015) 35–47.

[36] H. E, K. E. MacArthur, T. J. Pennycook, E. Okunishi, A. J. D'Alfonso, N. R. Lugg, L. J. Allen, P. D. a. Nellist, Probe integrated scattering cross sections in the analysis of atomic resolution HAADF STEM images, Ultramicroscopy 133 (2013) 109–119. doi:http://dx.doi.org/10.1016/j.ultramic.2013.07.002.

[37] R. Ishikawa, A. R. Lupini, Y. Hinuma, S. J. Pennycook, Large-angle illumination STEM: Toward three-dimensional atom-by-atom imaging, Ultramicroscopy 151 (2015) 122–129.

[38] K. H. W. van den Bos, A. De Backer, G. T. Martinez, N. Winckelmans, S. Bals, P. D. Nellist, S. Van Aert, Unscrambling mixed elements using

high angle annular dark field scanning transmission electron microscopy, Physical Review Letters 116 (2016) 246101.